Reprinted from

PHOTOGRAMMETRY & REMOTE SENSING

ISPRS Journal of Photogrammetry & Remote Sensing 53 (1998) 17–38

SAR image simulation and analysis of alpine terrain

M. Gelautz [a,*], H. Frick [a,1], J. Raggam [b], J. Burgstaller [a], F. Leberl [a,2]

[a] *Institute of Computer Vision and Graphics, Technical University Graz, Muenzgrabenstraße 11, A-8010 Graz, Austria*
[b] *Joanneum Research, Institute for Digital Image Processing, Wastiangasse 6, A-8010 Graz, Austria*

ELSEVIER

ELSEVIER

ISPRS Journal of Photogrammetry & Remote Sensing 53 (1998) 17–38

PHOTOGRAMMETRY
& REMOTE SENSING

SAR image simulation and analysis of alpine terrain

M. Gelautz [a,*], H. Frick [a,1], J. Raggam [b], J. Burgstaller [a], F. Leberl [a,2]

[a] *Institute of Computer Vision and Graphics, Technical University Graz, Muenzgrabenstraße 11, A-8010 Graz, Austria*
[b] *Joanneum Research, Institute for Digital Image Processing, Wastiangasse 6, A-8010 Graz, Austria*

Received 18 February 1997; accepted 24 July 1997

Abstract

We describe the implementation of a so-called object–space algorithm to use a digital elevation model (DEM) and a sensor flight path as input for the production of simulated SAR images. The method aims to achieve a high geometric accuracy and employs a parametric mapping model based on SAR range and Doppler equations. Information about SAR layover and shadow areas is stored in a so-called 'layover and shadow map'. We simulate ERS-1, X-SAR, and JERS-1 images of high-relief terrain, and compare them with corresponding real images. Manual measurements on the ERS-1 image show a simulation accuracy of better than 25 m, if sufficiently accurate sensor parameters are available. A cosine reflectance model delivers a good overall radiometric impression. However, this is being improved where ground truth exists, most notably on glaciers and areas covered with snow. As an application, we discuss the use of the simulated products for geometric rectification and radiometric calibration as a prerequisite for thematic analysis.

Keywords: remote sensing; SAR; simulation; layover; shadows; matching

1. Introduction

The analysis of radar images of highly accentuated terrain will greatly benefit from a software tool to simulate such images from known topographic data. We therefore have developed such a simulation tool and demonstrate its usefulness with various applications in alpine terrain.

Due to a classification introduced by Marconi (1984) and adopted by Leberl (1990), we can distinguish among three different methods of SAR image simulation, namely (a) a coherent 'system simulation', (b) an incoherent 'image simulation', and (c) a SAR image-based simulation. A simulation of type (a) would first simulate the raw SAR signal, i.e. the signal received on board before any processing, and then pass the signal through an appropriate SAR signal processor to produce the final SAR image. Examples of this technique include the 'end-to-end' simulator discussed by Camporeale and Galati (1991), the SARAS simulator described by Franceschetti et al. (1992), and the SAMOTRACE software package used by Polidori (1995). Contrary to that, simulators belonging to group (b) use the knowledge of the local incidence angle to compute the pixels of the output SAR image directly, without intermediate

* Corresponding author. Tel.: +43 (316) 873-5031; Fax: +43 (316) 873-5050; E-mail: gelautz@icg.tu-graz.ac.at
[1] Present address: Vexcel Corporation, 4909 Nautilus Court, Boulder, CO 80301, USA.
[2] Currently on leave at the Austrian Research Centre Seibersdorf, A-2444 Seibersdorf, Austria.

0924-2716/98/$19.00
PII S0924-2716(97)00028-2

raw signal simulation. That means that this method does not model how the SAR processing is actually carried out, which leads to a significant reduction in computing time. The simulations described by Domik (1985) and Guindon (1993) belong to this group. Finally, simulators which are classified as (c) combine an incoherent simulation with information extracted from an actual SAR image to compute a simulated image of another imaging configuration. This technique is adopted by Kimura and Kodaira (1993), who use AIRSAR data to simulate ERS-1 and JERS-1 images of the same test site, but was also used previously, for example by Domik and Leberl (1987). Rather than a separate class, method (c) can also be regarded as a sub-category of (b).

The implementation of a SAR simulation program in this paper is based on the approach of incoherent image simulation. The system was designed for applications in moderate to rugged terrain, where image grey values are mainly influenced by topography, rather than thematic content. Therefore, the main design goal was to achieve high geometric precision, as opposed to accurate modelling of a wide variety of ground classes. We review the system, several aspects of the geometric and radiometric modelling, and some computational issues. Then, tests are carried out on ERS-1, X-SAR, and JERS-1 images of the Oetztal test site in Tyrol (Austria). Two different backscatter models are employed, namely (a) a simple cosine reflectance function, and (b) a model which accounts for the effects of different types of terrain cover.

We find that the simulations based on the cosine model already deliver quite a realistic impression. The incorporation of ground truth leads to a further radiometric improvement, especially in areas covered with snow. We visualize the geometric precision of the simulation by superposition of real with simulated layover areas. An analysis shows that after manual refinement of the SAR sensor parameters the geometric deviations between the real and simulated image can be described by an rms error of less than 25 m. We also demonstrate the use of the simulated layover maps as a tool in the analysis and application of radar images, thus as a support means for SAR image interpretation, for example in the automated real–simulated image matching.

2. Previous work

The need for image simulation arises in various radar remote sensing tasks. One application is the planning of future radar missions, where the effects of different mapping configurations can be studied by simulation. For example, Kaupp et al. (1983) used simulation to investigate the influence of different stereo intersection angles on human stereo-viewing, and Domik (1985) carried out experiments with varying squint angles. Kobrick et al. (1986) report on a study with crossing flight paths. More recently, a planning tool for SAR data acquisition was proposed by Guindon (1993) to be based on image simulation. The author envisions a scenario where a user requests a simulation to better understand the effects of different possible viewing geometries. These simulated images can then be used to select that acquisition mode which best suits the user's needs.

Simulated images have been used by several authors for the geocoding of SAR images. First, match points between the real and simulated image have to be determined. Then, these match points, together with the known geometric relationship between the simulated image and DEM, are used to geocode the real image. An early work on real–simulated image matching for geocoding was presented by Guindon and Maruyama (1986). Kwok et al. (1990) report on experiments with two matching techniques, namely two-dimensional normalized cross-correlation on the one hand, and binary correlation of Marr-Hildred zero-crossings of the image on the other hand. A modification of conventional cross-correlation is proposed by Guindon (1995), who uses a similarity measure based on relative grey value rankings, rather than absolute grey values. Kimura and Iijima (1990) investigate in their work the influence of the chosen backscatter model on the matching performance, as well as the effects of speckle filtering. A study on the use of terrain-induced shadows as features for matching was presented by Leberl (1990). Wivell et al. (1992) also match real with simulated imagery to detect deviations of the sensor ephemeris from the ideal flight path.

The development of new image processing and feature extraction algorithms broadens the need for the application of simulated images, as they provide inexpensive and flexible test material. An example

by Thomas et al. (1989) reports initial tests of a multiple image SAR shape-from-shading algorithm that is built on the use of simulated images. A particular need for simulation arises when dealing with planetary data, due to the lack of ground truth. This is demonstrated by Wiles and Forshaw (1993), who employ simulated imagery as test data for a correlation algorithm developed for the automated detection of volcanoes on Venus from images acquired by NASA's Magellan probe.

So-called slope-effect-reduced radar images were created by Domik et al. (1988). In the original radar images, grey values are strongly influenced by topography; slope-effect-reduced images show mainly thematic information, as opposed to topographic content. Such images present the difference between a real and corresponding synthetic image, whose backscatter model is derived from image statistics. Recent research by Goering et al. (1995) uses radar images taken from ascending and descending orbits to calculate the parameters of an analytical backscatter model, which accounts for both diffuse and specular components. Tilley and Bonwit (1989) deal with an extreme case of terrain-induced distortions, namely layover. Their idea is to employ information stored in a simulated layover database for an inversion of the imaging process, thus generating a layover-corrected SAR image by proper redistribution of the energy compressed in the layover areas.

A very specific need for simulation presented itself in the planning of NASA's Magellan Mission to planet Venus, and the subsequent analysis of its images. For some areas on the Venusian surface three different kinds of radar imagery, namely two left-looking and one right-looking image, are available, as reported by Saunders et al. (1992). Stereo matching of the two images acquired from the same side delivers a DEM, which, however, cannot be checked for correctness, since no reference DEM of sufficient resolution is available for Venus. Using the computed DEM as input to a simulation program, with the sensor parameters taken from the opposite-side image, delivers a simulated image which can be compared to the real image for correctness, thus providing information about the accuracy of the computed DEM. Furthermore, the discrepancies between the real and simulated image can be used in a next step to refine the DEM.

3. Requirements of a simulation system

3.1. Geometric requirements

3.1.1. Geometric accuracy

A main design goal was to achieve high geometric accuracy. Therefore, a precise modelling of the sensor flight path was necessary, and a rigorous mapping model based on SAR range/Doppler equations ('parametric mapping model') was chosen, optionally taking into account the Doppler effect induced by the rotation of the Earth. Moreover, curvature of the Earth and other geodetic aspects are considered through the use of rigorous cartographic transformations. This is opposed to the simulators described by Domik (1985) and Guindon (1993), who assume constant sensor altitude and heading and use a simplified mapping model.

3.1.2. Layover and shadow map

When dealing with steep slopes in the terrain, the computation of a so-called 'layover and shadow map' becomes an important requirement. This map, which can be computed in both image and DEM geometry, contains information on the location of layover and shadow areas. In our examples, layover areas are displayed in white, whereas shadows are marked as black regions. Pixels which were classified as both layover and shadows are displayed as layover, according to their appearance in the real SAR image. One possible application of such a map is to mask those areas of an image where the radiometric information is not reliable. As further applications, we demonstrate its use for accuracy analysis, as well as the automated acquisition of tie points between the real and simulated image.

3.2. Radiometric requirements

3.2.1. Radiometric accuracy

Aiming primarily at simulations of an alpine environment, where topographic effects are stronger than thematic influences, we employ as first backscatter model a simple cosine function. As a refinement, a second backscatter function was implemented, which models the effects of several classes of terrain cover often found in mountainous areas. Contrary to applications in flat terrain, special effects such as multiple

reflections arising in built-up areas, or the proper modelling of texture related to agricultural patterns need not be considered.

3.2.2. Speckle noise

For those applications in which simulated images are used as test data instead of real imagery, SAR speckle needs to be incorporated into the simulation, in order to provide test images which look as realistic as possible. This is to avoid situations in which newly developed image processing algorithms perform well in first tests on simulated data, however fail afterwards in their actual application to real SAR data.

3.3. Computational efficiency

A final major goal was computational speed. Therefore, special attention was paid to an efficient implementation of the developed algorithms.

3.4. Data inputs to and results from the simulation

From the geometric point of view, the required input is a DEM and a sensor flight path, which is given as a series of sensor positions with corresponding time information. From these discrete sensor positions a continuous flight path is derived by fitting a low-order polynomial. Further input parameters are range and time information in terms of an offset and scaling factor, slant-to-ground-range conversion parameters, as well as wavelength and Doppler parameters.

Regarding radiometry, first the desired backscatter model has to be chosen. If the simulation should also account for different types of terrain and land use, a ground cover map related to the DEM geometry is a further requirement.

Output of the program is a simulated SAR image, as well as layover and shadow maps in both DEM and image geometry. Further products available to the user are a local incidence angle map, a look angle map, and an illuminated DEM, which are generated as by-products during the simulation process.

4. Geometric model

4.1. Establishing the geometric relationship

From a geometric point of view, two different approaches may be used to create a simulated (SAR) image, both being based on the input of a DEM and proper modelling of the sensor flight path, range, and Doppler parameters.

(1) Transformation of DEM points to corresponding line and column coordinates of the simulated image (so-called object–space approach). This creates an irregular raster of resulting points in the image space, which has to be postprocessed in order to generate a regular image raster as well as appropriate layover and shadow areas.

(2) Transformation of simulated image raster points to ground points through intersection of the SAR range/Doppler projection 'circle' with the surface of the DEM (so-called image–space approach). Thereby the entire regular raster of the simulated image is created with simultaneous detection of layover pixels, whereas the detection of SAR shadow areas requires a proper postprocessing step.

It is obvious that the intersection of range/Doppler equations and DEM surface within the second approach is rather complex and, therefore, time-consuming, in particular if the DEM is considered in an arbitrary cartographic presentation, whereas the calculations have to be made in a cartesian system.

Hence, for a first implementation of a SAR simulation software the object–space approach was selected, since one of the primary design goals was computational speed. The simulation module was embedded into the Remote Sensing Software Package (RSG, 1993), as this software package provides useful prerequisites like point transformation libraries, polynomial fitting by least-squares methods, etc.

After performing some necessary coordinate transforms, the mapping from DEM to image space is conceptually done by determining for each DEM point the sensor position at the moment when this point was imaged. Once the sensor position is known, the SAR image coordinates, i.e. the range and azimuth values, can be easily calculated. The algorithm used is briefly outlined in the following. For a more detailed description see Raggam et al. (1993).

Starting points are the two basic SAR mapping equations, namely the Doppler (F_D) and range (F_r) equations:

$$F_D = \lambda f_{DC}/2 - \vec{p} - \vec{s}(p - s)|\vec{p} - \vec{s}| = 0 \quad (1)$$

$$F_r = r - |\vec{p} - \vec{s}| = 0 \quad (2)$$

where $\vec{p} = (X, Y, Z)^T$ is the position of the DEM point to be transformed, and $\vec{s} = (X_s(t), Y_s(t), Z_s(t))$ the location of the sensor when this point was imaged. The corresponding velocity vectors are $\dot{\vec{s}}$ and $\dot{\vec{p}}$, the latter one compensating for Earth rotation. In the imaging model we employ, the sensor flight path s is approximated by a low-order polynomial, which means that $X_s(t)$, $Y_s(t)$ and $Z_s(t)$ are polynomial functions of the imaging time t. The slant range value r gives the distance between a DEM point and the corresponding sensor position. Parameter λ denotes the radar wavelength. The Doppler frequency shift f_{DC} is a function of range and azimuth values, which for our purpose was approximated by a second-order polynomial. In the case of zero-Doppler processed images, f_{DC} equals zero. Range and azimuth resolution, which were input to the simulation program, are now used to establish a relationship between the physical radar image coordinates r and t on the one side, and the SAR image coordinates x and y on the other side. After these transforms, both F_D and F_r can be regarded as functions of the unknown variables x and y. However, the equations are nonlinear, and can therefore not be solved directly.

The solution is obtained iteratively, by applying the Newton method. Under the assumption that a start value (x_0, y_0) is available, linearization of the SAR mapping equations is achieved by using the linear terms of a Taylor expansion. This delivers:

$$F_D(x_0, y_0) + \frac{\partial F_D}{\partial x} \cdot \Delta_x + \frac{\partial F_D}{\partial y} \cdot \Delta_y = 0 \quad (3)$$

$$F_r(x_0, y_0) + \frac{\partial F_r}{\partial x} \cdot \Delta x + \frac{\partial F_r}{\partial y} \cdot \Delta y = 0 \quad (4)$$

The above linear equations can now be solved directly for the unknown variables Δ_x and Δ_y. Adding (Δ_x, Δ_y) to (x_0, y_0) delivers a new start value for the next iteration step. The iteration stops when the refinement values Δ_x and Δ_y meet the imposed accuracy requirements. As start value (x_0, y_0) for the first iteration loop, the image coordinates computed for the previous DEM point are used.

In addition to the computed image position (x, y) (thus giving range and azimuth value), information about the corresponding look angle α and the incidence angle Θ (the angle between the incident radar wave and the local surface normal) is also stored for each DEM point. They are later used to calculate the image grey values and shadow map.

4.2. Radar layover and shadows

In order to provide a better understanding of the problems encountered, the radar-specific phenomena 'layover' and 'radar shadows' are briefly reviewed in Fig. 1. There, it is shown how the special radar imaging geometry, which is based on range measurements, leads to geometric distortions in the resulting image. Layover occurs in those cases where the top of the mountain is closer to the sensor than the bottom, i.e. the terrain is sufficiently steep. Layover areas appear in the image as bright regions with the original geometric order being disturbed. Similar to optical images, those areas which are not 'illuminated' by the radar beam are called radar shadows. Shadow areas appear in the image as dark regions corrupted by thermal noise. In radar image simulation, layover and shadows require special consideration, because in both cases the individual points of the input DEM cannot be regarded independently of each other, but terrain points lying within a certain neighbourhood need also be taken into account.

From a theoretical point of view, we can distinguish between two types of shadow regions, namely active and passive shadows. Active shadows are those parts of the terrain which are not illuminated by the radar beam because the local incidence angle exceeds 90°. On the other hand, areas which do not receive energy because of some obstacle between the sensor and the terrain surface are denoted as passive shadows. Similarly, active layover areas are those which cause layover because the terrain slope exceeds the local sensor look angle, whereas passive layover areas are only affected by layover because of an adjacent active layover. When dealing with layover and shadow maps, it should be noted that the distinction between active and passive shadows can be made in both DEM and image geometry. For layover, however, this distinction is only possible in DEM geometry. A more thorough discussion of active vs. passive layover and shadows, as well as possible interactions between them, can be found in Kropatsch and Strobl (1990).

The shadow detection algorithm we use in our implementation delivers both active and passive shad-

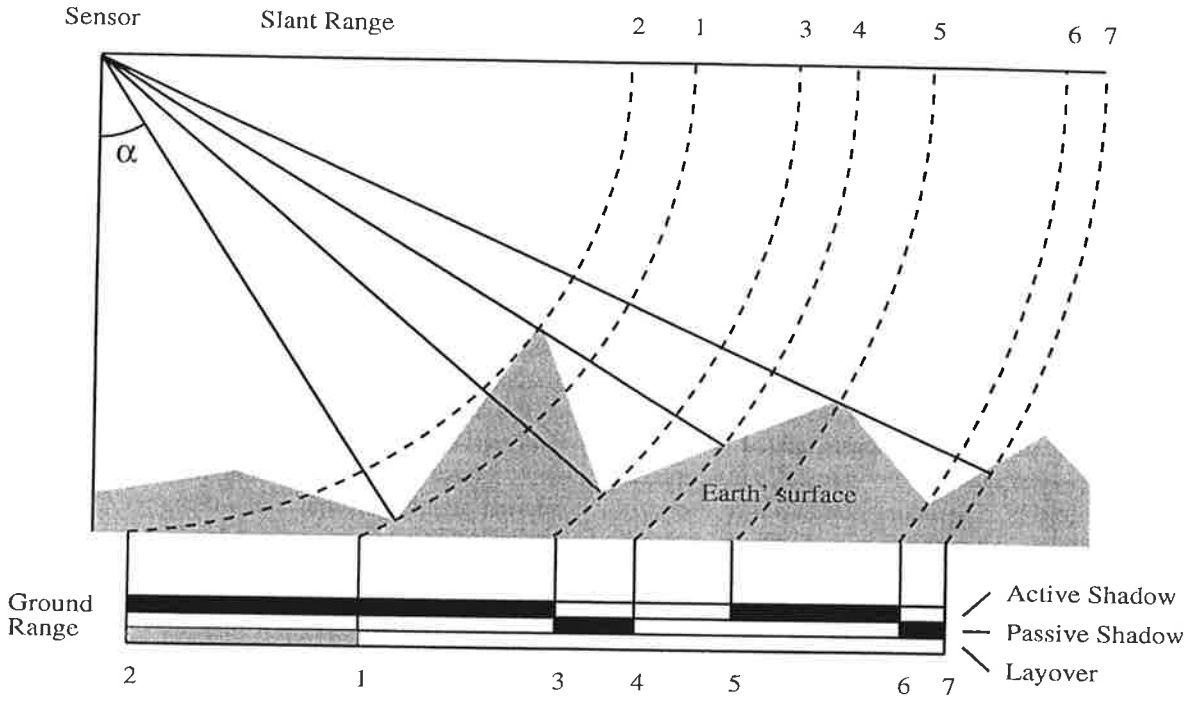

Fig. 1. Illustration of layover and radar shadows (after Schreier, 1993).

ows, without distinguishing between them. Its principle can be seen from the cross-section through mountainous terrain shown in Fig. 1. From a walk along that profile, beginning from near range, shadows can be determined as follows. Following the relief to the far range, the look angle α must increase monotonously, or shadowing occurs. Should we find that the look angle decreases as we proceed away from the nadir point of the radar system, then we have found a surface point in shadows.

A characteristic of layover areas is that each point in image space receives energy reflected from multiple parts of the terrain in object space. In the algorithm we implemented, the detection of layover is a by-product of the image resampling process, with hardly any additional computing burden; those pixels in image space which during the resampling process are found to be covered by more than one DEM cell are marked as belonging to a layover region. This is opposed to an algorithm as suggested by Meier et al. (1993), who propose a technique similar to the previously described shadow extraction for a combined detection of both layover and shadows in DEM geometry. The advantage of a separation into a rather time-consuming shadow computation on the one side, and a fast layover calculation on the other side becomes obvious in applications where due to a priori knowledge about the imaging scenario the occurrence of shadows can be precluded. In such a case, the shadow computation, which — depending on the computer architecture used — can take up to 40% of the overall simulation time, can be entirely skipped. Since with this technique layover is first determined in image geometry, the layover map in DEM geometry is then obtained by mapping back to DEM space.

4.3. Geometric resolution or pixel size

A further important point to be discussed is the relationship between the resolution of the input DEM and output SAR image. Commercially available DEMs, such as the one we use for our test site, typically exhibit a resolution in the range of 25 m to 100 m. Having in mind the simulation of images acquired by sensors such as ERS-1, JERS-1, and X-SAR, with associated pixel sizes of down to 12.5 × 12.5 m, we aim at simulating images with

a comparable or higher resolution than the corresponding DEM. However, due to the decrease in SAR ground range resolution associated with foreshortening and layover, we also have to cope with situations in which image resolution is lower than DEM resolution.

The method proposed by Guindon (1993) to overcome this problem relies on oversampling the DEM by an appropriate factor, so that image resolution is always lower than DEM resolution. However, this approach is not applicable in our case, since, due to our assumption of an arbitrary sensor flight path, the mapping from DEM to image space carried out for each DEM point is quite a time-consuming operation. Therefore, oversampling the DEM and mapping the resulting DEM points would lead to prohibitive computing times, especially for larger scenes. This means that in our implementation we have to distinguish between the following two cases: (a) image resolution is higher than DEM resolution, and (b) image resolution is lower than DEM resolution. In (a) the energy reflected from one DEM cell has to be distributed among the image pixels covered by that cell, whereas in (b) the energy of the DEM cells falling into one image pixel has to be summed up. This redistribution of energy is related to the radiometric considerations discussed in the next section.

5. Radiometric model

5.1. Image grey values

Generally, the grey value at each image pixel is determined by the power returned to the radar from that area of the DEM which corresponds to the relevant pixel. Following the notation used by Leberl (1990), the return power σ can be split into two components A and σ_0, namely:

$$\sigma = A \cdot \sigma_0 \tag{5}$$

with A being the so-called area effect. This effect is caused by the variation in ground range resolution discussed in the previous section. The value σ_0 represents the radar backscatter coefficient, which depends on various factors such as surface properties (e.g. material, roughness, moisture content), local incidence angle, wavelength and polarization.

In our implementation, two different models were used for computing σ_0. The first, simplified approach assumes that an analytical expression is available for σ_0. This allows the computation of σ_0 as a function of the local incidence angle Θ and further constant coefficients. For the analytical backscatter function we chose a cosine function, which originally derives from modelling a Lambertian surface. Further examples of often used analytical backscatter models are the formulae developed by Hagfors (1964) and Muhleman (1964) in the context of astronomical applications. The second approach we employ provides a more rigorous treatment, as it accounts for the dielectric properties of different types of terrain. The computation of σ_0 in this case is explained in more detail below.

Once the image intensity values are thus computed, and SAR layover and shadows are properly considered, a final conversion using a square root or logarithmic function may be required, according to the sensor type to be simulated.

5.2. Ground truth

In order to incorporate thematic information, we used reflectance functions which were derived from experimentally determined backscatter curves, as given by Ulaby and Dobson (1989). The coefficients which describe σ_0 for different types of terrain cover as a function of the local incidence angle are stored in a database. If for a given combination of ground class, wavelength and polarization the required coefficients were not available, the values of a similar class were chosen as an approximation. In some cases, efforts were made to further improve the realistic appearance by additional fine-tuning of the original parameters. According to the requirements of an alpine environment, the currently implemented classes are:

- water
- forest
- alpine vegetation
- rock
- snow

A future extension to the simulator for applications in flat terrain is planned. Then, further classes of terrain and vegetation, e.g. different kinds of agricultural use and built-up areas, will be included.

5.3. Speckle

The two speckle generation algorithms we use in our simulation are described in more detail by Bolter et al. (1996), and therefore are only briefly summarized here. The first method is based on a Rayleigh distribution, with multiple file averaging in order to account for multiple looks. The second approach uses a χ^2 distribution with 2 N degrees of freedom, with N being the number of independent looks. According to Ulaby et al. (1982), the use of a Rayleigh distribution models the properties of a linear detector in the SAR processing system, whereas the χ^2 distribution reflects the behaviour of a square-law detector. Strictly speaking, both models are only valid under the assumption of a homogeneous area. The kind of probability distribution applicable to heterogeneous areas is still a subject of investigation, as stated by Huang and van Genderen (1996). However, this problem arises mainly when simulating relatively flat areas with different types of vegetation and land use, and can therefore be neglected in our current implementation.

6. Software structure

From an implementational point of view, the simulation software is preferably divided into three modules, as shown in Fig. 2. In the first module, the necessary *geometric calculations* and the shadow detection are carried out. The geometry files contain, for each DEM point, that location in the SAR image onto which this particular point is mapped. The *radiometric calculations* performed in the second module use a chosen backscatter model or ground cover map to convert the information available in a local incidence angle map into a file containing the backscattered energy. Finally, the *resampling* module performs the resampling in the image space, after consideration of the area effect. The layover

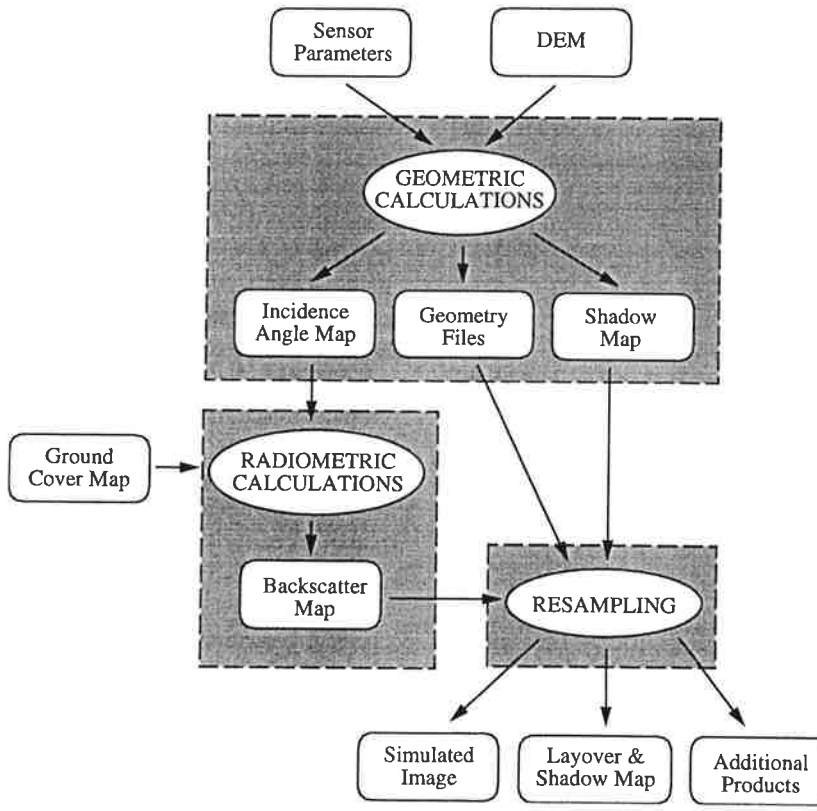

Fig. 2. Overview of the modular structure of the simulation program.

detection is also done at this stage. The modular structure of the software has the advantage that if the same scene is simulated several times with different backscatter models, only the radiometry and resampling modules have to be invoked again, whereas the rather time-consuming geometric computations are carried out only once.

7. Simulation results

7.1. The data sets

In order to evaluate the geometric and radiometric accuracy of our simulator, we generated synthetic ERS-1, X-SAR, and JERS-1 images, and compared them to the corresponding real data. Some characteristics of our test data are given in Table 1. In the following, some of the simulated images and derived products are shown, and the results obtained from the ERS-1 simulation are presented and analyzed in more detail.

Table 1
Overview of test images

	ERS-1	X-SAR	JERS-1
Spectral band	C	X	L
Polarization	VV	VV	HH
Look angle (°)	23	50	35
Acquisition orbit	ascending	ascending	descending
Doppler	no	no	yes

The input terrain model consists of a 1030 × 640 DEM of the Oetztal, an X-SAR/SIR-C 'super-test-site' which is located in the Austrian Alps, close to the Italian border. The resolution of the DEM is 25 × 25 m. The whole area exhibits strong topographic relief, with elevations ranging from 1750 m to more than 3750 m. The DEM was produced by digitizing contour lines of topographic maps in a scale of 1 : 25,000. Fig. 3 shows the illuminated DEM. A further input to the simulator was the corresponding ground cover map, which can be seen in Fig. 4. The map we use exhibits a resolution of 50 × 50 m, and shows five different classes (water, forest, alpine vegetation, rock, and glacier). The missing information in the southern part of the area is due to the fact that for our study ground truth was only available for the Austrian part of the territory.

7.2. ERS-1

The real ERS-1 image, whose imaging parameters were used for the simulation, can be seen in Fig. 5a. The image was acquired in September 1992. The

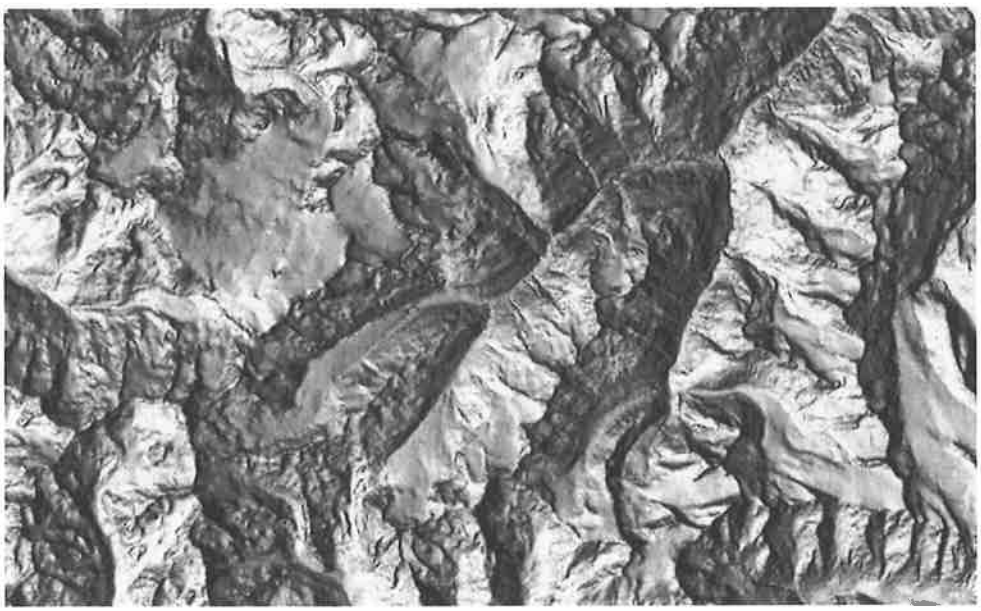

Fig. 3. DEM of the Oetztal, Tyrol, illuminated from the ERS-1 sensor position. Area size is approx. 26 × 16 km.

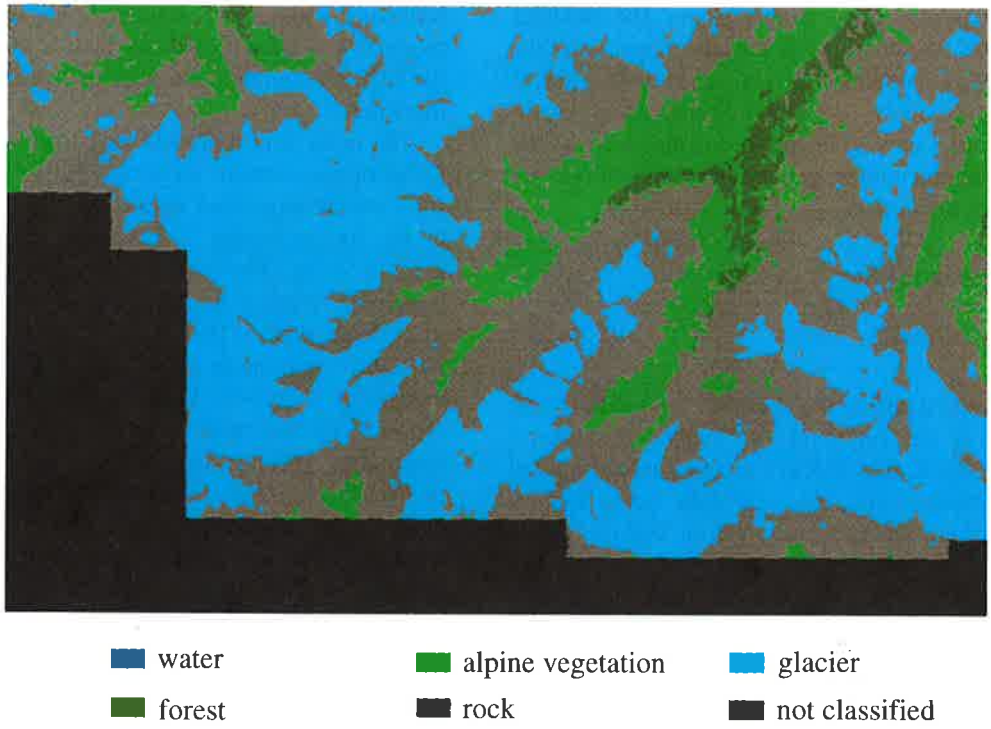

Fig. 4. Ground cover map of the Oetztal test site. The area covered corresponds to the DEM from Fig. 3.

sensor was flying to the left of the image (ascending orbit), with a look angle of 23°. The result of the simulation based on the cosine reflectance function is given in Fig. 5c. Comparison with the corresponding 'snow and ice map' in Fig. 5d shows that radiometric differences between (a) and (c) are most clearly visible on snowfields or glaciers. In these areas, the result of the cosine-based simulation tends to be too bright in comparison to surrounding regions. Fig. 6a was obtained after incorporating ground truth and SAR speckle (in those areas where no ground truth was available, as indicated in Figs. 4 and 5d, the cosine function was used as default value). The detailed views in Fig. 6b–d illustrate the effects of adding simulated speckle noise. A first visual comparison between Figs. 5 and 6 shows a high geometric accuracy and quite a good radiometric impression of the simulated image in Fig. 5c, which is further improved in Fig. 6a. Fig. 5b shows the computed layover and shadow map in image geometry. Due to the steep look angle of the ERS-1 sensor, layover areas predominate and practically no radar shadows occur. For illustration purposes, the layover map in DEM geometry was superimposed on the illuminated DEM. The result can be seen in Fig. 7a. Comparison with Fig. 3 illustrates which parts of the terrain are affected by layover. Approximately 30% of the terrain was classified as belonging to layover regions.

7.3. X-SAR

A real X-SAR image of the Oetztal test site is shown in Fig. 8a. The scene was acquired in October 1994, during an ascending orbit. The scene was illuminated from the left, with a look angle of 50°. The simulation results obtained from the cosine model and the incorporation of thematic information can be seen in Fig. 8, b and c, respectively. The rather shallow look angle of the sensor leads to some radar shadows (6%), whereas hardly any layover regions can be found (1%). Fig. 8d shows the layover and shadow map in image geometry. A visualization of those parts of the terrain which are affected by shadows is given in Fig. 7b.

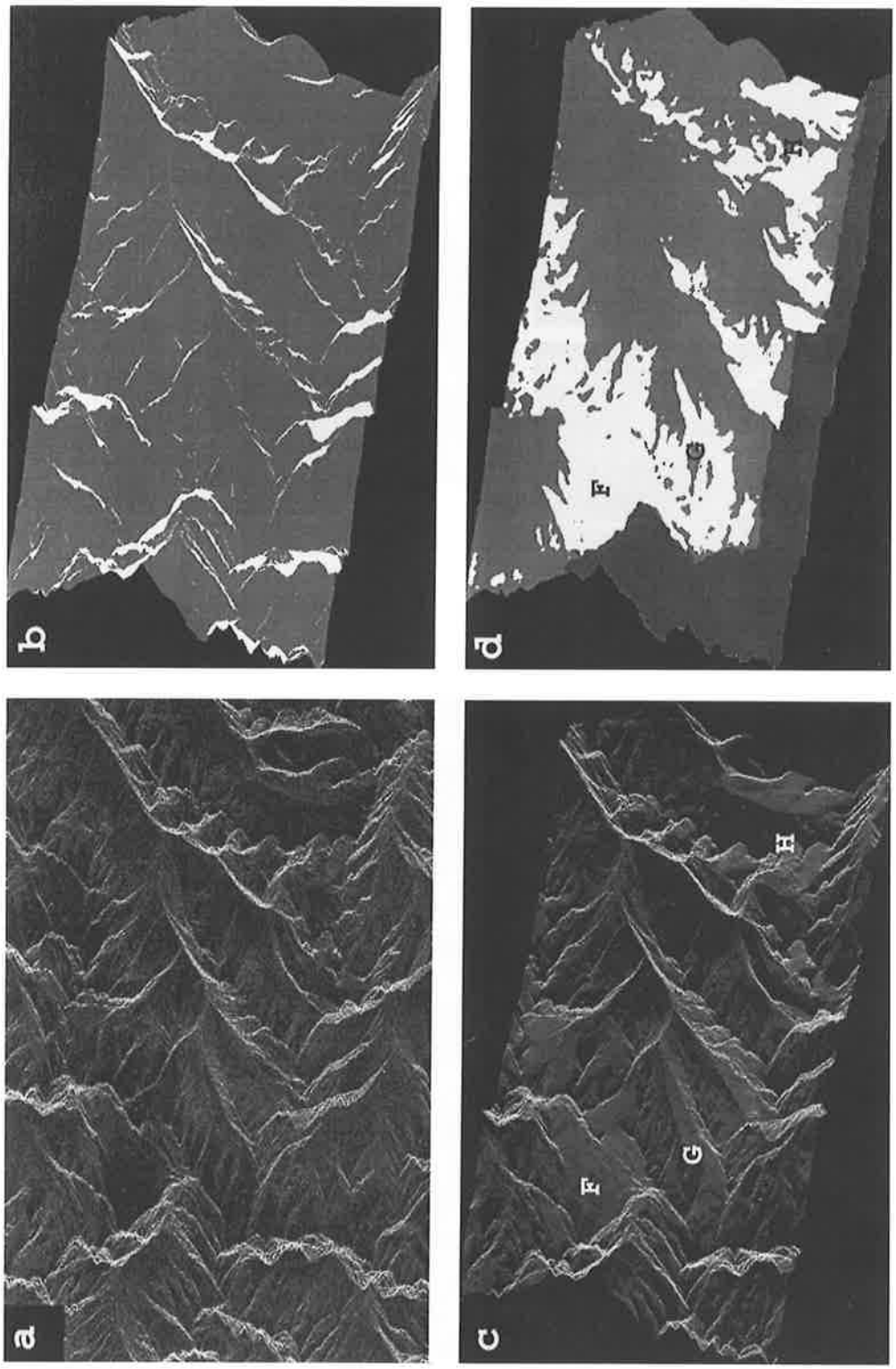

Fig. 5. (a) ERS-1 image of the Oetztal area, covering approx. 600 km^2 ©esa. (b) Layover and shadow map in image geometry. Layover areas are marked as bright regions. (c) Simulated image corresponding to the real image from (a). A cosine function was used as reflectance model. (d) Snow and ice cover map in image geometry, generated by simulation from Fig. 4. Snow and ice regions are displayed in white, and areas of missing ground truth are shown in dark grey. Several corresponding points (F, G, H) are marked in (c) and (d) for orientation.

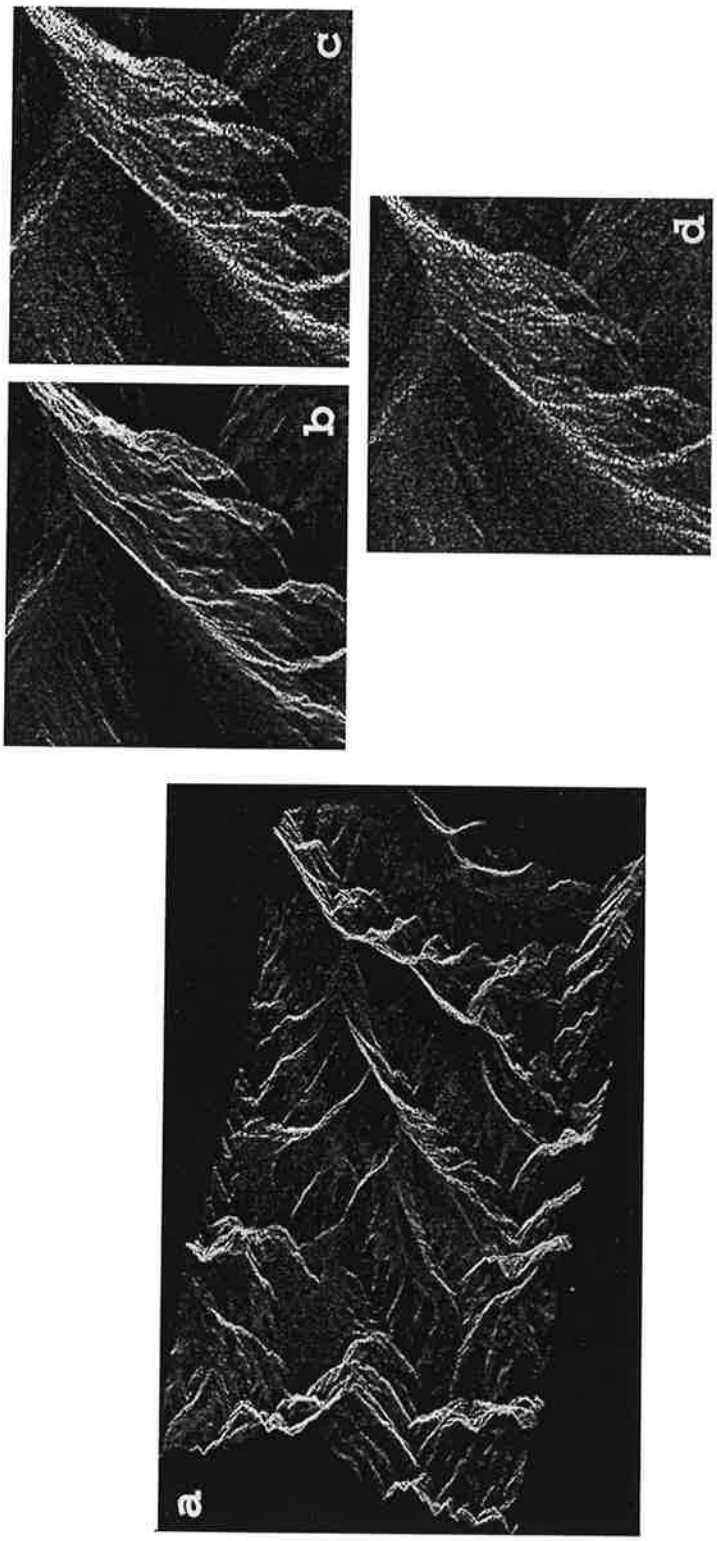

Fig. 6. The simulated ERS-1 image, with thematic information included and speckle noise superimposed, is shown in (a). An image detail before (b) and after (c) adding SAR speckle, and the corresponding section of the real image (d).

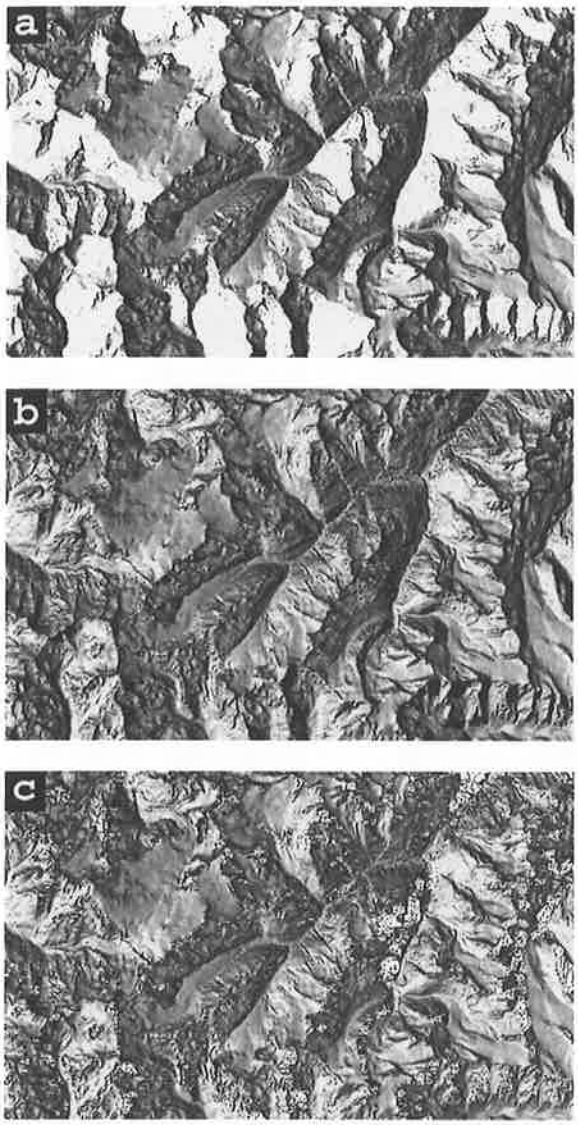

Fig. 7. Comparison of layover and shadows caused by different sensors. The simulated layover and shadow maps obtained for ERS-1 (a), X-SAR (b), and JERS (c) are overlaid onto the illuminated DEM from Fig. 3. Layover areas are displayed in white, shadows are marked in black.

7.4. JERS-1

As opposed to the ERS-1 and X-SAR examples given above, the JERS-1 image shown in Fig. 9a was taken during a descending orbit, with an off-nadir look angle of 35°. Fig. 9b shows the corresponding synthetic image obtained from the cosine-based simulation, whereas ground truth is modelled in Fig. 9c. The layover and shadow areas in the image and DEM geometry can be identified with the help of Fig. 9d and Fig. 7c, respectively. An analysis has shown that 6% of the terrain is affected by layover, and 1% is lying in SAR shadows. Table 2 summarizes the layover and shadow effects caused by the three sensors.

Table 2
Percentage of terrain affected by layover and shadows

	ERS-1	X-SAR	JERS-1
Look angle (°)	23	50	35
Layover (%)	30	1	6
Shadows (%)	0	6	1

8. Performance analysis

8.1. Geometric analysis

In order to determine the potential accuracy of the simulation, an analysis was performed on the simulated ERS-1 image. As the geometric differences between the real and simulated image do not only reflect the precision of the simulation itself, but are also strongly influenced by insufficient knowledge of the sensor position and SAR processing parameters, the first step was a manual refinement of the input parameters delivered by the SAR processing facility. Then, the simulation was carried out, and manually acquired control points between the real and simulated image were used to determine the remaining distortions between the two images. The measurements were made at salient features in the image, mainly at the edges of foreshortening and layover areas. Based on a set of 18 control points distributed across the image, it was found that the relationship between the two images could be described by a mere translation, with an rms error of less then ± 25 m or ± 2 pixels. In terms of the original ERS-1 resolution of 25 m (before resampling to 12.5 m), this corresponds to an rms error of less than ± 1 pixel. This figure includes also the effects of errors in the DEM, as well as any remaining sensor parameter deviations which were not compensated for by the manual adjustment, and can therefore be regarded as an upper boundary of the simulation accuracy.

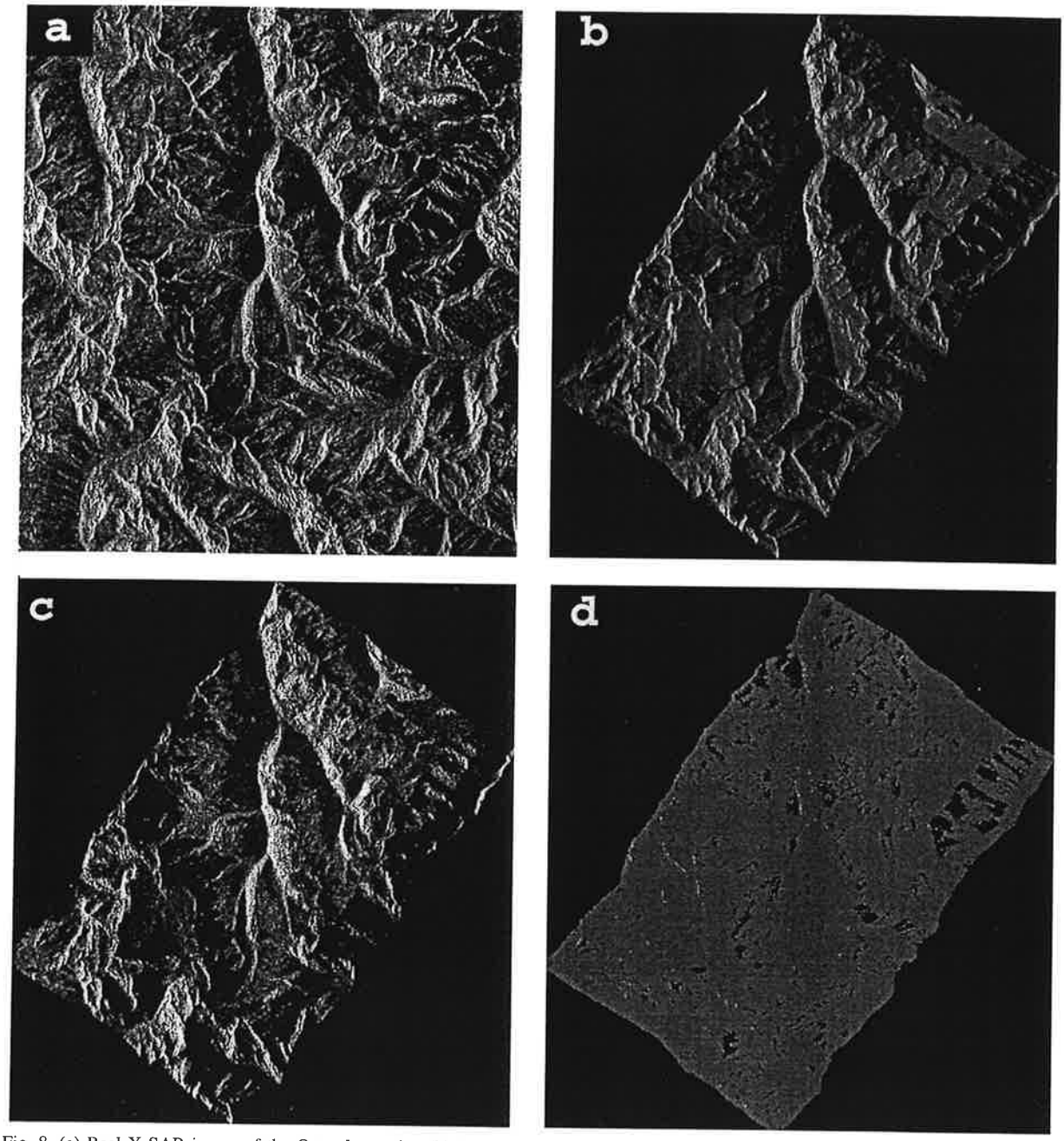

Fig. 8. (a) Real X-SAR image of the Oetztal test site. (b) The corresponding simulated image, generated by using a cosine backscatter model. (c) Simulation accounting for the effects of both terrain cover and SAR speckle. (d) Layover and shadow map in image geometry.

Visual inspection of the accuracy can be achieved with the help of the layover map. From the real SAR image in Fig. 5a, the presumed layover regions were extracted by thresholding (see Fig. 10a). A suitable threshold value was determined by using the percentage of layover pixels in the layover map from Fig. 5b. Now, the maps from Fig. 5b and Fig. 10a were superimposed, according to the

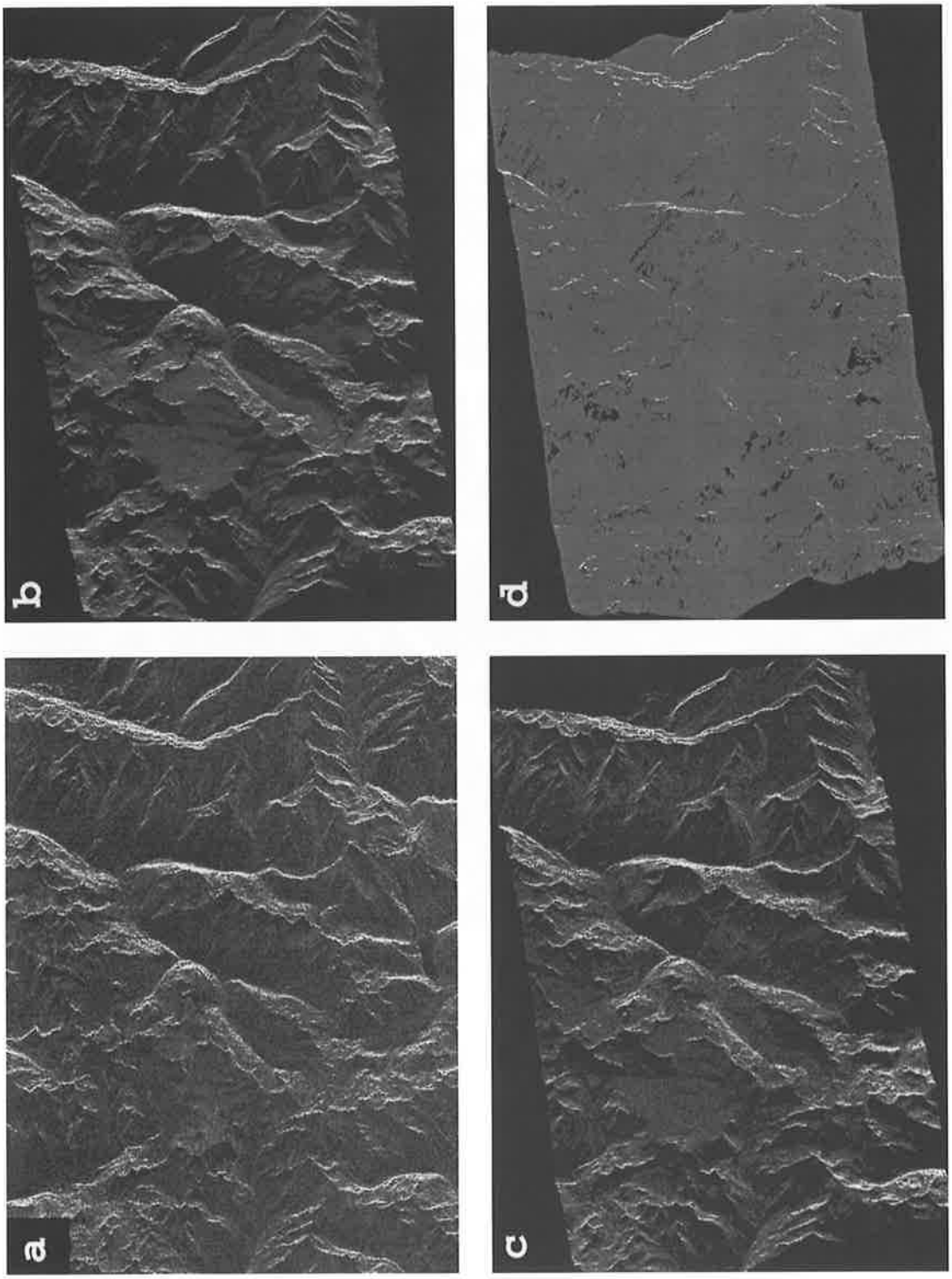

Fig. 9. (a) JERS-1 image of the Oetztal area, acquired in October 1993. The sensor was flying to the right of the image. Simulation results obtained from a cosine law (b), and after incorporating ground truth and speckle (c). The layover and shadow map in image geometry is shown in (d).

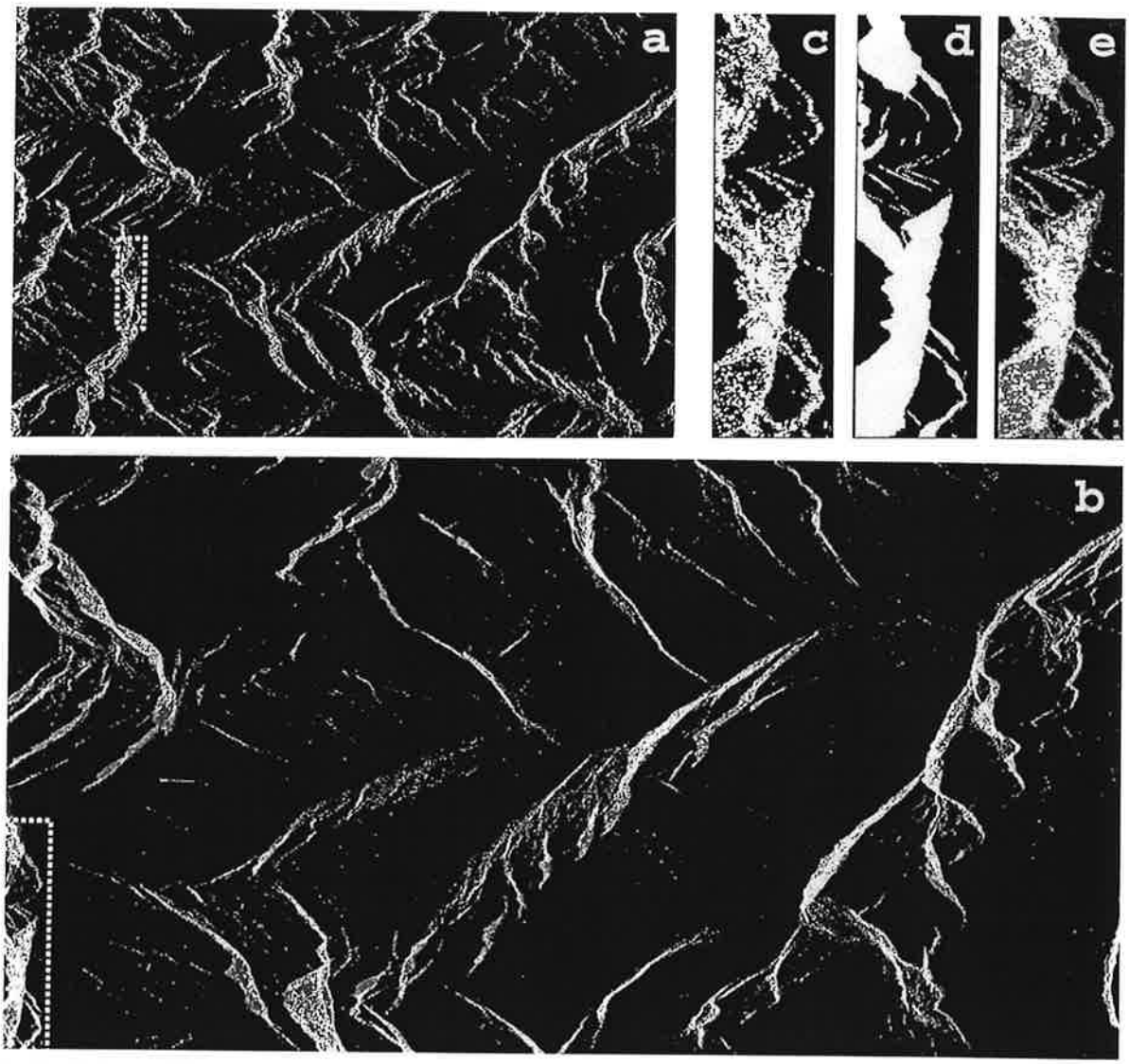

Fig. 10. (a) Supposed layover areas extracted by thresholding from Fig. 5a. (b) Binary overlap of the layover areas from (a) and Fig. 5b. The overlap illustrates the high geometric accuracy of the simulation. A detailed view of the real image after binarization, the corresponding section of the layover map, and the overlap result are given in (c), (d), and (e), respectively.

previously determined offset between the real and simulated image. The result can be seen in Fig. 10b, where white pixels indicate layover in both masks, and grey pixels in only one of them. Despite deviations due to speckle and varying terrain reflectivity, very good coincidence between the general outline of the real and simulated features can be observed, which demonstrates the high precision of the simulation.

8.2. Radiometric analysis

For the simulated data of the ERS, X-SAR and JERS SAR sensors, the radiometric analysis in a first step was based on visual comparison and interpretation. In this regard it has to be noted that the test site is a high-mountainous area in the Austrian Alps leading to extreme geometric distortions inherent to the SAR imaging dispositions. For this test area it

could be demonstrated that the use of the cosine reflectance model already delivered quite useful and realistic results, as in such rugged terrain the impact of the topography on the SAR backscatter values dominates in comparison to the impact of the ground cover. In all of our examples, the cosine-based image (see Fig. 5c, Fig. 8b and Fig. 9b) shows a good correspondence when compared to the real SAR image. The main radiometric differences can be detected in snow-covered and glaciated areas, as can be seen from inspecting Fig. 5a, c and d. However, for subsequent purely geometry-based applications — such as identification of tie points — these simulation products are absolutely sufficient, as corresponding features in the simulated and real image can easily be identified.

As for the more realistic simulation products being based on the incorporation of ground cover information, the achieved results are very promising. The visual comparison shows an almost perfect correspondence between the real and simulated image for the ERS and JERS experiment. Hence we can conclude that for the C- and L-frequency bands the backscatter functions which have been used in the simulation are very applicable, at least for those ground cover types being considered. In comparison, the result achieved for the X-band X-SAR sensor is still markedly worse. Particularly, the radiometric similarity of some glacier areas is significantly decreased. Moreover, a difference in the similarity of simulated fore- and backslopes is obvious. This leads us to the conclusion that the X-band backscatter functions still need some fine-tuning in order to improve the simulated X-SAR image.

8.3. Computation time

Using a 1030 × 640 input DEM, the computation on a SUN Sparc station Ultra-1 with 143 MHz and a memory size of 64 Mb took less than 10 min. The overall computation time can be split up as follows:

- Geometric calculations and shadow detection 6 : 05 min
- Radiometric calculations 0 : 09 min
- Resampling and layover detection 3 : 15 min

A further speed-up of the algorithm could be achieved by parallelization. Due to memory constraints, several parts of the code (e.g. shadow detection) use the principle of data decomposition already in the current serial implementation. The exploitation of this hidden parallelism in a future parallel implementation appears to be promising.

9. Matching a SAR image to a DEM

We now demonstrate the use of the simulated products for matching a SAR image to a DEM. An ERS-1 scene (descending orbit) of the Oetztal area was chosen for illustration. As input to the simulator, the parameters obtained from the SAR processing facility were used; no previous manual refinement was carried out.

The first approach relies on matching the real with the simulated grey value image. As matching algorithm, we used the software developed by Frankot et al. (1994). The algorithm is based on hierarchical cross-correlation of image grey values, and was specially designed for SAR imagery corrupted by speckle noise. An internal confidence value derived from the shape of the correlation surface serves to filter out bad matches. An example of automatically determined real–simulated match points can be seen in Fig. 11. The numbers shown there (generated as internal numbering by the matching software when applied to a larger section) help to identify corresponding points in the left and right image. A first visual evaluation of the matching results shows no clearly discernible mismatches. Similar results were obtained from further tests on other ERS-1 and X-SAR data. We therefore conclude that our simulated images resemble their real partners closely enough that the automated acquisition of tie points is feasible.

For those cases where a sufficient amount of layover/shadows is available all across the image, we propose as a second approach the use of SAR layover and shadows as features for matching. The idea of employing shadow areas for automated tie pointing has been previously proposed by Leberl (1990). In that work, investigations concentrate on exploiting shadow boundaries. Contrary to that, tests with ERS-1 and X-SAR images have shown that due to the high local geometric precision of our simulation a simple binary overlapping technique could be applied successfully to determine automatically the offset between the real and simulated

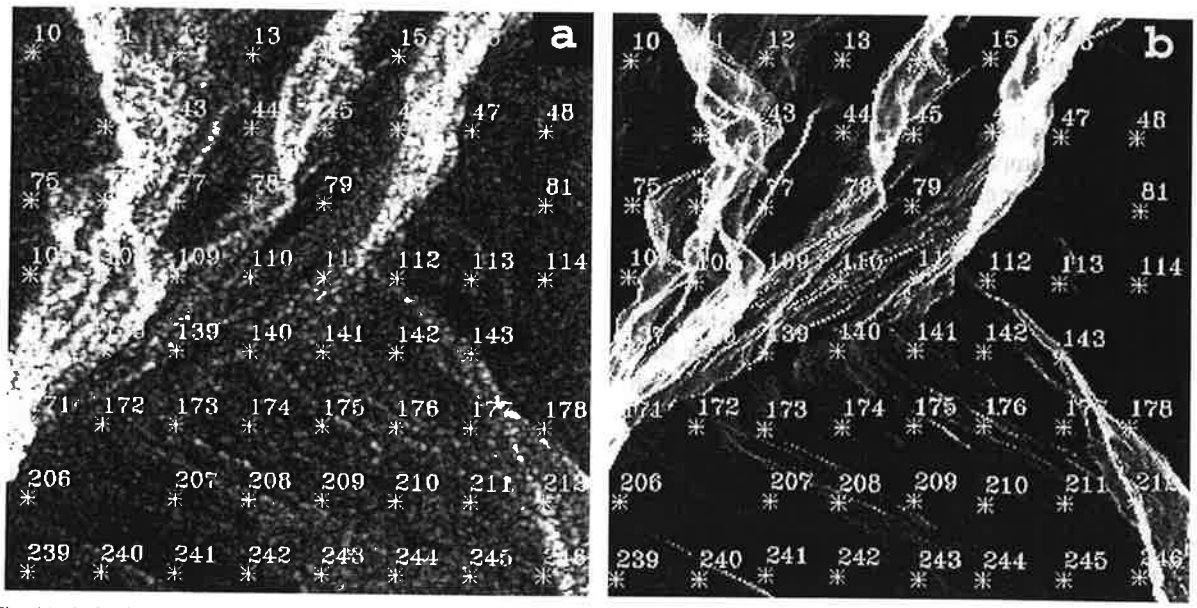

Fig. 11. A detail of a real (a) and corresponding simulated (b) ERS-1 scene, with automated match points superimposed. The simulation employed a cosine reflectance model.

layover/shadow regions. The obvious advantages of this straightforward technique, as opposed to a more complex approach based on boundary characteristics, are easy implementation, reduced computing burden, and robustness to SAR speckle.

The superposition of the real and simulated layover regions at the location of the maximum overlap can be seen in Fig. 12a, b. The corresponding correlation surfaces are given in Fig. 12, c and d, respectively. Note that there is a clear peak in the correlation surface, which indicates the validity of this approach. Further investigations are currently being carried out in order to automate the selection of suitable subwindows, and to determine which degree of distortion between the real and simulated image can be applied in this approach.

Once tie points between the real and simulated images have been collected, the geocoding can be carried out. The match points can either serve to compute directly an appropriate transform between the DEM and SAR image, or first be employed in an intermediate step to refine the SAR sensor parameters. Fig. 13 shows an example set of the final geocoded SAR images and additional products delivered by our simulator, as may be used for monitoring snow/ice cover in an alpine environment (e.g. for hydrological investigations). The geometrically rectified X-SAR (a) and ERS-1 (b) images were generated by projecting the SAR image grey values onto the map geometry. Pixel brightness in the geocoded images is therefore influenced by both thematic and topographic components. A local incidence angle map, which is computed as a by-product during the simulation process, could be utilized in a next step to eliminate the influence of the area effect on the image grey values, as a first step towards the radiometric calibration of the SAR image (see, e.g. Zyl et al., 1993, or Raney et al., 1994). For illustration, Fig. 13c shows the incidence angle map for the X-SAR image from Fig. 13a. In SAR layover areas, the removal of the area effect — although theoretically possible — has to rely on assumptions about the backscatter model, and can therefore only be approximate. As a consequence, no radiometrically calibrated image can be recovered in these regions. A layover and shadow map in DEM geometry — shown in Fig. 13d for the ERS-1 image from Fig. 13b — indicates to the user which areas should be excluded from subsequent thematic interpretation. As an example, attempts could then be made to extract the snow cover from a geometrically and radiometrically corrected SAR data set,

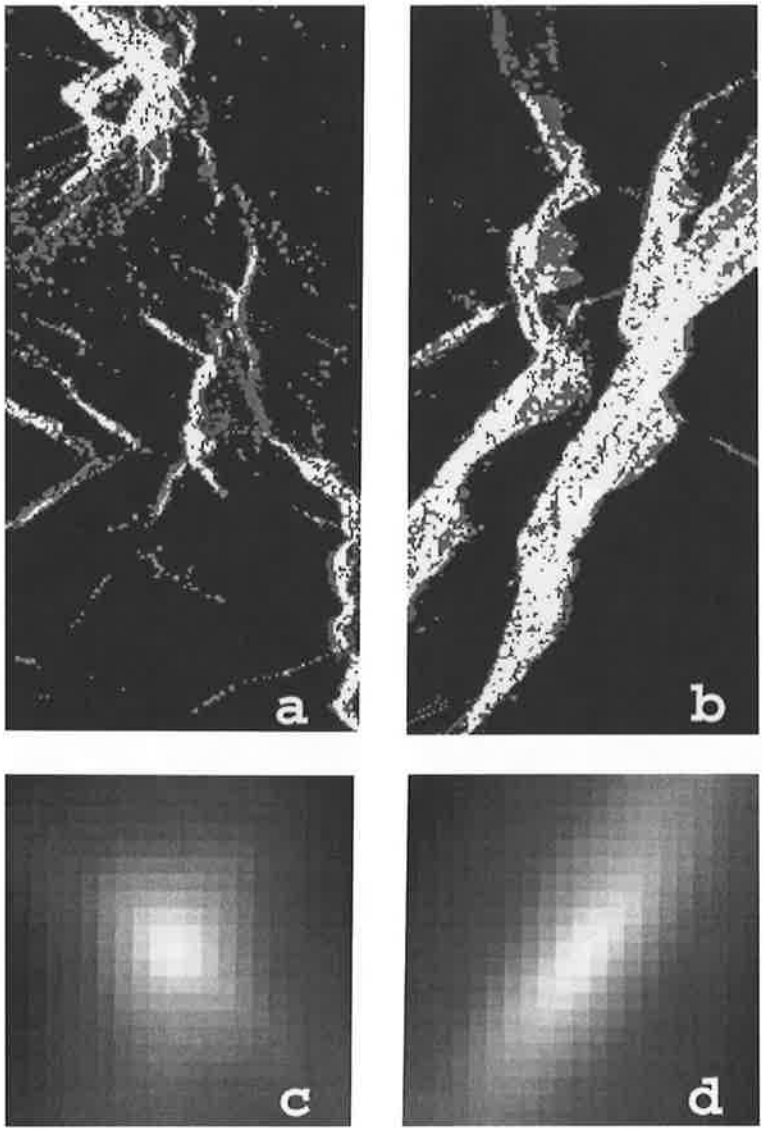

Fig. 12. Positions of maximum binary overlap are shown in (a) and (b). Overlapping pixels are displayed in white. The corresponding grey value encoded correlation surfaces are shown in (c) and (d) .

optionally acquired by different sensors. Temporal changes can be detected through a comparison with snow cover reference data, e.g. as given in Fig. 4.

10. Summary and outlook

We have described the implementation of a SAR simulation program which uses a DEM, sensor flight path and further SAR processing parameters to compute the output SAR image directly, without intermediate raw signal representation. In order to achieve high geometric precision, a rigorous mapping model based on the SAR range/Doppler equations was employed. Furthermore, particular attention was paid to the computational efficiency of the implemented algorithms. The current implementation is specially suited to applications in alpine terrain, where SAR layover and shadows occur frequently. Therefore, the generation and utilization of layover and shadow maps has been discussed in some detail. Tests were

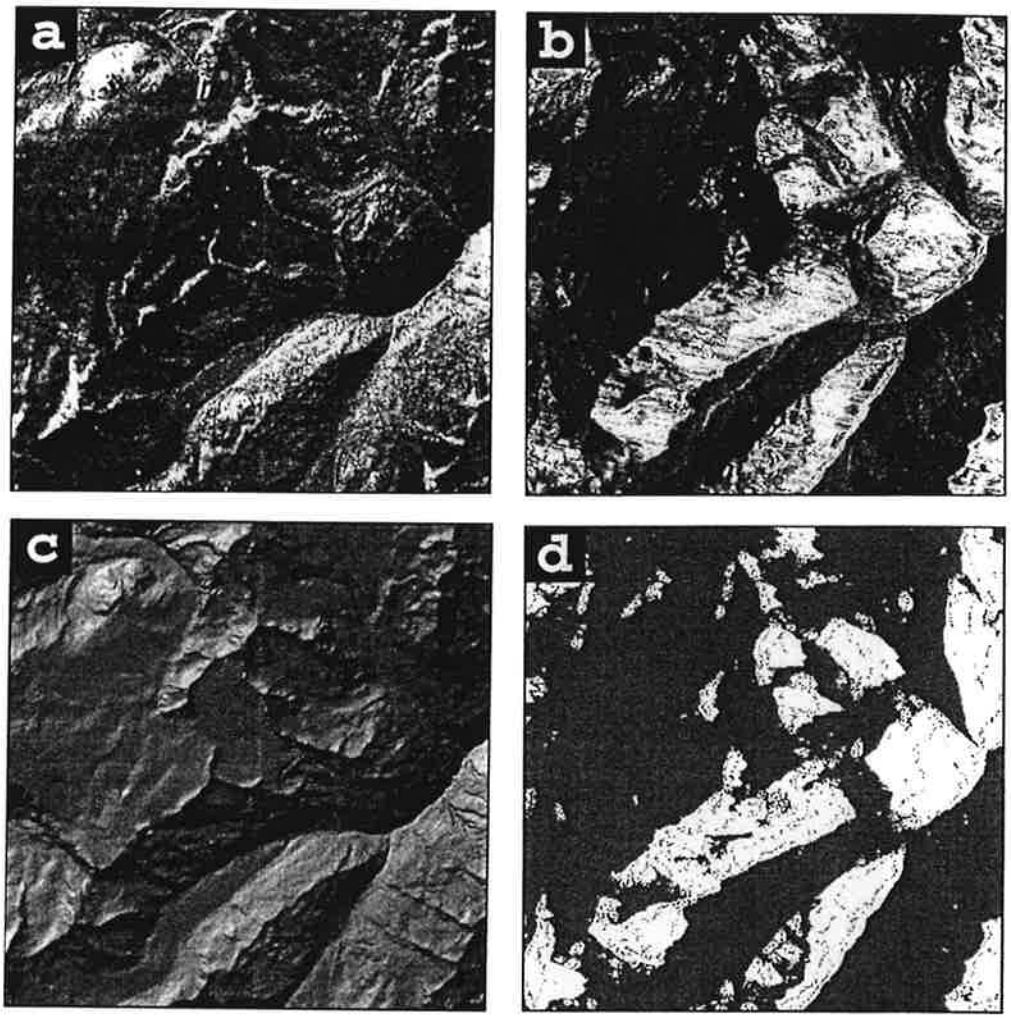

Fig. 13. Illustration of a geocoded data set and additional simulated products useful for glaciological studies. The geocoded X-SAR (ascending orbit) and ERS-1 image (descending orbit) are shown in (a) and (b), respectively. Subfigure (c) gives the grey value encoded local incidence angle map corresponding to (a). The layover map in (d) marks the layover regions from (b).

carried out on SAR images obtained from different sensors (ERS-1, X-SAR, and JERS-1), and the simulation results were judged by comparison with the corresponding real images. An accuracy analysis performed on the ERS-1 image has shown that after manual tuning of the simulation input parameters and rms error of less than ±25 m could be achieved. Regarding the radiometric appearance, especially the simulated ERS and JERS images were found to resemble their corresponding real partners remarkably well, whereas the employed X-band backscatter model would still require some fine-tuning in order to generate X-SAR simulations of comparable quality. The improvement obtained from the incorporation of thematic information, as opposed to the use of a simple cosine backscatter model, was most pronounced in glaciated areas. As an example of a practical application, we demonstrated the use of the simulated images and layover/shadow maps for the automated acquisition of tie points.

The immediate next step will be to carry out further tests on real–simulated image matching. The match points obtained from the real and simulated grey value images by applying a correlation-based algorithm will be compared to the results of the binary overlapping technique. The influence of the-

matic information, as opposed to the assumption of a Lambertian surface, on the accuracy of the matching results will also be investigated.

As a future extension to the simulator, the incorporation of further ground classes such as different types of vegetation, traffic lines, and built-up areas is planned. Then the simulation could be used for automated ground control point measurement, as mentioned above, even in flat terrain.

Acknowledgements

The authors wish to thank S. Hensley from NASA/JPL for providing his matching software. The ERS-1 and X-SAR data were obtained from Dr. H. Rott from the Institute for Meteorology and Geophysics at the University of Innsbruck. Dr. Rott is Principal Investigator of the AO/Experiment A1 and the SIR-C/X-SAR Mission. We gratefully acknowledge his cooperation. Further thanks go the Institute for Photogrammetry and Remote Sensing at the Vienna University of Technology for providing the ground cover map.

References

Bolter, R., Gelautz, M., Leberl, F., 1996. SAR speckle simulation. Int. Arch. Photogramm. Remote Sensing 21 (B2), 20–25.

Camporeale, C., Galati, G., 1991. Digital computer simulation of synthetic aperture systems and images. Eur. Trans. Telecommun. Related Technol. 2 (3), 343–352.

Domik, G., 1985. Verfahrensentwicklungen zur Analyse von digitalen Seitsicht-Radarbildern gebirgigen Geländes mittels digitaler Höhenmodelle und Bildsimulation. Doctoral Thesis, Graz University of Technology.

Domik, G., Leberl, F., 1987. Image based SAR product simulation. Proc. American Society of Photogrammetry and Remote Sensing, 53rd Annu. Conv., Baltimore, MD, pp. 355–364.

Domik, G., Leberl, F., Cimino, J., 1988. Dependence of image grey values on topography in SIR-B images. Int. J. Remote Sensing 9 (5), 1013–1022.

Franceschetti, G., Migliaccio, M., Riccio, D., Schirinzi, G., 1992. SARAS: A synthetic aperture radar (SAR) raw signal simulator. IEEE Trans. Geosci. Remote Sensing 30 (1), 110–123.

Frankot, R., Hensley, S., Shafer, S., 1994. Noise resistant estimation techniques for SAR image registration and stereo matching. Proc. IGARSS '94, Pasadena, CA, pp. 1151–1153.

Goering, D., Chen, H., Hinzman, L., Kane, D., 1995. Removal of terrain effects from SAR satellite imagery of Arctic tundra. IEEE Trans. Geosci. Remote Sensing 33 (1), 185–194.

Guindon, B., 1993. Development of a SAR data acquisition planning tool (SARPLAN) based on image simulation. Int. J. Remote Sensing 14 (2), 333–344.

Guindon, B., 1995. Performance evaluation of real–simulated image matching techniques in the acquisition of ground control for ERS-1 image geocoding. ISPRS J. Photogramm. Remote Sensing 50 (1), 2–11.

Guindon, B., Maruyama, H., 1986. Automated matching of real and simulated SAR imagery as a tool for ground control point acquisition. Can. J. Remote Sensing 12 (2), 149–158.

Hagfors, T., 1964. Backscattering from an undulating surface with applications to radar returns from the Moon. J. Geophys. Res. 69 (18), 3779–3784.

Huang, Y., van Genderen, J., 1996. Evaluation of several speckle filtering techniques for ERS-1 and 2 imagery. Int. Arch. Photogramm. Remote Sensing 21 (B2), 164–169.

Kaupp, V., Bridges, L., Pisaruck, M., MacDonald, H., Waite, W., 1983. Simulation of spaceborne stereo radar imagery: experimental results. IEEE Trans. Geosci. Remote Sensing GE-21 (3), 400–405.

Kimura, H., Iijima, T., 1990. Automated matching of real and simulated SAR imagery for geometric correction. Proc. IGARSS '90, Vol. 1, pp. 309–312.

Kimura, H., Kodaira, N., 1993. Simulation and comparison of JERS-1 and ERS-1 SAR images. Proc. IGARSS '93, Vol. 4, pp. 1774–1776.

Kobrick, M., Leberl, F., Raggam, J., 1986. Radar stereo mapping with crossing flight lines. Can. J. Remote Sensing 12, 132–148.

Kropatsch, W., Strobl, D., 1990. The generation of SAR layover and shadow maps from digital elevation models. IEEE Trans. Geosci. Remote Sensing 28 (1), 98–107.

Kwok, R., Curlander, J., Pang, S., 1990. An automated system for mosaicking spaceborne SAR imagery. Int. J. Remote Sensing 11 (2), 202–223.

Leberl, F., 1990. Radargrammetric Image Processing. Artech House, Norwood, MA, 595 pp.

Marconi, 1984. SAR simulation concept and tools. Final Report, Marconi Research Centre, Chelmsford, Essex, UK, Report MTR 84/34, 109 pp.

Meier, E., Frei, U., Nuesch, D., 1993. Precise terrain corrected geocoded images. In: Schreier, G. (Ed.), SAR Geocoding — Data and Systems. Wichmann Verlag, Karlsruhe, pp. 173–185.

Muhleman, D., 1964. Radar scattering from Venus and the Moon. Astron. J. 24, 34–41.

Polidori, L., 1995. On the use of SAR image simulation for the validation of topographic mapping techniques. EARSeL Workshop on Topography from Space. Adv. Remote Sensing 4 (2), 40–48.

Raggam, J., Strobl, D., Hummelbrunner, W., 1993. Product quality enhancement and quality evaluation. In: Schreier, G. (Ed.), SAR Geocoding — Data and Systems. Wichmann Verlag, Karlsruhe, pp. 187–206.

Raney, R., Freeman, T., Hawkins, R., Bamler, R., 1994. A plea for radar brightness. Proc. IGARSS '94, Pasadena, CA, pp. 1090–1092.

RSG, 1993. RSG — Remote Sensing Software Package Graz.

Joanneum Research, Software User Manual, Release Nr. 3.0, Institute for Digital Image Processing.

Saunders, R., Spear, A.J., Allin, P.C., Austin, R.S., and 23 others, 1992. Magellan mission summary. J. Geophys. Res. 97 (E8), 13067–13090.

Schreier, G., 1993. Geometrical properties of SAR images. In: Schreier, G. (Ed.), SAR Geocoding — Data and Systems. Wichmann Verlag, Karlsruhe, pp. 103–134.

Thomas, J., Kober, W., Leberl, F., 1989. Multiple image SAR shape-from-shading. Proc. IGARSS '89, pp. 592–596.

Tilley, D., Bonwit, K., 1989. Reduction of layover distortion in SAR imagery. Remote Sensing Environ. 27, 211–220.

Ulaby, F., Dobson, M., 1989. Handbook of Radar Scattering Statistics for Terrain. Artech House, Norwood, MA, 357 pp.

Ulaby, F., Moore, R., Fung, A., 1982. Microwave Remote Sensing: Active and Passive. Vol II: Radar Remote Sensing and Surface Scattering and Emission Theory. Ulaby, F. (Ed.), Artech House, Norwood, MA, pp. 484–487.

Wiles, C., Forshaw, M., 1993. Recognition of volcanoes on Venus using correlation methods. Image Vision Comput. 11 (4), 188–196.

Wivell, C., Steinwand, D., Kelly, G., Meyer, D., 1992. Evaluation of terrain models for the geocoding and terrain correction of synthetic aperture radar (SAR) images. IEEE Trans. Geosci. Remote Sensing 30 (6), 1137–1144.

Zyl, J., Chapman, B., Dubois, P., Shi, J., 1993. The effect of topography on SAR calibration. IEEE Trans. Geosci. Remote Sensing 31 (5), 1036–1043.